Journal of Catalysis **205,** 266–277 (2002)
doi:10.1006/jcat.2001.3456, available online at http://www.idealibrary.com on IDEAL®

Correlated Atomic Resolution Microscopy and Spectroscopy Studies of $Sn(Sb)O_2$ Nanophase Catalysts

K. Sun,*,[1] J. Liu,† and N. D. Browning*

*Department of Physics, University of Illinois at Chicago, 845 W. Taylor St., Chicago, Illinois 60607-7059; and †Monsanto Company, 800 N. Lindbergh Blvd., St. Louis, Missouri 63167

Received May 18, 2001; revised October 12, 2001; accepted October 12, 2001

A series of antimony-doped tin oxide (ATO), $Sn(Sb)O_2$, nanophase catalysts (containing 43 mol% Sb calcined at temperatures of 250, 600, and 1000°C, respectively) have been studied by correlated electron energy-loss spectroscopy (EELS) and *Z*-contrast imaging in a scanning transmission electron microscope (STEM) and by high-resolution electron microscopy (HREM). As reference materials, pure SnO_2, Sb_2O_3, and Sb_2O_5 are also analyzed. Results show that the particle size of these ATO catalysts increases with the calcination temperature. At low calcination temperatures, the catalyst contains crystalline nanoparticles surrounded by amorphous material, while the nanoparticles become well crystallized when calcined at higher temperatures. EEL spectra acquired from these ATO catalysts are qualitatively interpreted using 'fingerprints' from the reference materials. Results suggest that at low calcination temperatures (250°C), Sb exists in the pentavalent state Sb (V) either incorporated into the SnO_2 lattice or as an amorphous layer surrounding the SnO_2 crystals. At higher temperatures (≥600°C), Sb segregation occurs as trivalent Sb (III) at the surface and Sb (V) in the core of the majority of the nanoparticles. However, it should be noted that nearly no Sb was detected in some particles. The surface Sb (III) ions are proposed as active sites in the ATO catalysts.

Key Words: **EELS; *Z*-contrast imaging; STEM; HREM; ATO; catalysts; valence state; nanophase materials.**

1. INTRODUCTION

Pure tin oxide (SnO_2) is used for either the deep oxidation (1) or the oxidative dehydrogenation (2) of lower olefins. When doped with antimony (Sb), it can be used for the oxidation of propylene to acrolein, the ammoxidation of propylene to acrylonitrile, the oxidative dehydrogenation of butanes to 1,3-butaliene (3), and for the selective oxidation of olefins (4). The difference in properties between ATO catalysts and pure SnO_2 implies that Sb plays an important role in ATO's catalytic performance. Understanding the structure–activity relationship of ATO catalysts is therefore of key technological importance.

Previously the structure of ATO catalysts was characterized by various spectroscopic techniques, such as X-ray photoelectron spectroscopy (XPS) (5–9), Mössbauer spectrometry (10–13), ultraviolet photoelectron spectroscopy (UPS), high-resolution electron energy-loss spectroscopy (HREELS) (7), infrared (IR), Raman, and Auger spectroscopy (14), X-ray fluorescence spectrometry (15), and X-ray absorption spectroscopy (XAS) (16). In addition X-ray diffraction (XRD) (5, 10, 14–16), neutron diffraction (17), transmission electron microscopy (15, 18–20), and extensive computer simulations (21) have been employed. However, despite this intensive effort, the distribution and the valence states of Sb in ATO catalysts have been the subject of debate for many years. It has been generally agreed that surface enrichment of antimony occurs, and trivalent Sb (III) ions are formed during calcination. Furthermore, at high calcination temperatures, tin (IV) oxide is thought to contain pentavalent Sb (V) within the bulk lattice and Sb (III) located at surface sites, although no direct experimental evidence for either of these features has been provided.

The majority of research into the valence states and distribution of Sb in ATO catalysts has utilized XPS and Mössbauer spectrometry. The advantage of these two techniques is that different oxidation states show separate core-level signals. However, XPS, like other surface techniques (HREELS, for example), samples only a thin surface layer of a solid material. It therefore needs to be performed in combination with other techniques, such as X-ray diffraction, to obtain bulk structure information. The poor crystallinity of technologically relevant materials in this case precludes accurate structural investigation by X-ray diffraction. Mössbauer spectrometry, like many other spectroscopic techniques, also cannot separate surface signals from bulk ones, thereby limiting the ability to determine the spatial distribution of the various valence states of Sb. While conventional microscopic imaging methods in TEM can give accurate estimates of particle size and crystallinity (i.e., the information missing from the spectroscopic techniques), they cannot give composition and electronic structural information.

[1] To whom correspondence should be addressed. Fax: 312-996-4451. E-mail: ksun@uic.edu.

0021-9517/02 $35.00

The limitations in the techniques described previously are that they only address one aspect of the problem at hand. Therefore, the best way to characterize atomic and electronic structures of nanoscale catalysts is to use a set of techniques where imaging and spectroscopic techniques can be performed simultaneously. One means of achieving this correlation is through *Z*-contrast imaging and EELS in the STEM (22). Electron energy-loss spectroscopy is a powerful technique used to investigate electronic structures of materials (23). EELS performed in a modern electron microscope has one advantage over X-ray spectroscopy and other techniques: it can be performed at atomic resolution. This makes it possible to individually analyze the atomic and electronic structures of nanoparticles, defects, and interfaces. Through the combination of *Z*-contrast and HREM imaging and EELS techniques, we can get not only size and crystallinity information but also composition and electronic structure data from individual nanoparticles.

In the research presented here, a series of ATO catalysts (containing 43 mol% Sb calcined at temperatures of 250, 600, and 1000°C, respectively) have been studied. Using *Z*-contrast images as references, EEL spectra were collected by placing the electron probe at both the edges and the centers of particles in the ATO catalysts. This is the first time that correlated atomic resolution electron microscopy and spectroscopy techniques were used for characterizing these types of catalysts. These spectra were qualitatively interpreted by fitting the spectra using the reference spectra collected from pure SnO_2, Sb_2O_3, and Sb_2O_5 materials through a multiple-linear-least-squares (MLLS) process, from which we directly probe the distribution and valence states of Sb in ATO catalysts calcined at different temperatures. HREM imaging was also used for analyzing the particle size and crystallization of the ATO catalysts.

2. EXPERIMENTAL METHODS

2.1. Sample Preparation

Wet chemical techniques were used to synthesize the ATO nanophase materials. A solution of $SnCl_4 \cdot 0.5\ H_2O$ (40.0 g) in deionized water (20 ml) was mixed with $SbCl_5$ (25.0 g) in concentrated HCl (20 ml), stirred, and heated; 15% sodium hydroxide solution was then added to keep the pH value of the final mixture at 2.0. At this point the heater was turned off, and the mixture, still being stirred, was allowed to cool for 3 h. The white solid precipitates were then filtered off, washed with deionized water, and dried at 60°C in a vacuum oven for more than 3 h. The dried powders were then calcined in an open ceramic crucible at 250, 600, and 1000°C, respectively, for 3 h. At the end of the calcination, the sample was removed from the oven and allowed to cool quickly in air. The final powders of ATO catalysts calcined at 250, 600, and 1000°C showed light gray, light green, and dark gray colors, respectively. Specimens for electron microscopy analysis were prepared by placing the powders directly on holey-carbon-coated copper grids.

2.2. Electron Microscopy and Spectroscopy

The methodology used in this study for characterizing the ATO nanophase catalysts involved combining atomic resolution imaging and spectroscopic techniques in the electron microscope. HREM (performed in a JEOL 3010 HREM) and *Z*-contrast imaging techniques were used to characterize particle size and crystallinity, while EELS combined with *Z*-contrast imaging was used for analysis of the valence states and the distribution of antimony. *Z*-contrast imaging and EELS were performed in a JEOL 2010F field emission STEM/TEM operating at 200 kV in STEM mode (22). The lens conditions in the microscope were defined for a probe size of 0.2 nm, with a convergence angle of 13 mrad and a collection angle of 52 mrad (24). The energy resolution of the energy-loss spectra was 1.2 eV (defined by the full-width at half-maximum of zero-loss peak) at a dispersion of 0.3 eV/channel. To reduce the effects of the beam damage, short acquisition times (0.2 s for low-loss spectra and 0.5 or 1 s for core-loss spectra) were used to collect individual spectra from all the materials analyzed, and then these spectra were summed up to increase the signal-to-noise ratio. In addition, a different collection manner was used, i.e., with the probe scanning continuously over a larger area. This acquisition method was suggested to avoid potential problems in interpreting the spectra due to beam damage (36). The Gatan PEELS system and EL/P 3.3 software were used for EELS data collection and processing.

Figure 1 shows a schematic diagram of the optical arrangement in a STEM. The key to the STEM is that electrons emitted from the gun are focused into a small probe (typically 0.13–0.3 nm). When the focused probe scans over the specimen, electrons are scattered in a large-range of angles. For *Z*-contrast imaging, only the high-angle scattered electrons are collected using an annular detector (25–28). Since the annular detector collects mainly thermal diffuse scattering, which is generated by each atom in proportion to the electron intensity close to its site, lateral coherence between the atomic columns is destroyed, and the coherence between atoms in the same column is reduced to residual. Therefore, each atom can be considered as an independent scatterer. Scattering factors may be replaced by cross sections; the cross section for HAADF scattering approaches the Rutherford cross section, thus approaching a Z^2 dependence on atomic number Z of the intensity. Therefore, there is no phase problem for *Z*-contrast imaging. This cross section effectively forms an object function that is strongly peaked at the atom sites

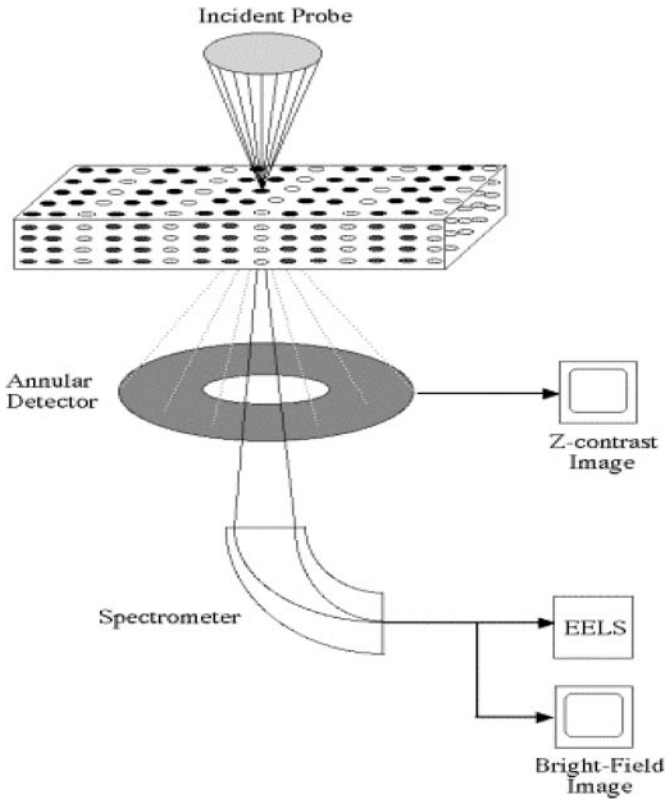

FIG. 1. Schematic diagram of the optical arrangement for Z-contrast imaging and EELS analysis using a scanned probe in the TEM.

($\sim$0.02 nm). Thus, for a very thin specimen when there is no dynamical diffraction, the scattered intensity ($I(R)$) can be written as

$$I(R) = O(R) \otimes P^2(R), \qquad [1]$$

where $O(R)$ is the object function and $P^2(R)$ is the probe function; i.e., the Z-contrast image can be considered as a simple convolution between the probe intensity profile and the specimen object function (25–28). The spatial resolution is only controlled by the probe size due to the small width of the object function. For thin crystalline materials in zone-axis orientations, if the probe size is smaller than the atomic column spacing, atomic columns can be illuminated individually, and atomic resolution Z-contrast images are obtained. This result also holds true for thicker specimens due to channeling effects (29).

Since the annular detector does not interfere with low-angle scattering, the low-angle scattering can be used for either EELS or bright-field imaging (Fig. 1). For the majority of edges accessible by conventional energy-loss spectrometers ($\Delta < 2$ keV) the object functions are localized within 0.1 nm of the atom core (23). Similarly, for crystalline materials in zone-axis orientations, the spectrum can also be described as a convolution of the probe with an object function similar to that of Z-contrast imaging, thereby atomic resolution EELS can be achieved (29–33).

The arrangement in Fig. 1 shows that atomic resolution EELS and Z-contrast imaging can be performed simultaneously; i.e., a spectrum is acquired by using the Z-contrast image to position the electron probe over a particular structural feature.

3. RESULTS

3.1. HREM Results

Figure 2a shows low magnification and Fig. 2b shows high-resolution images (along the [$\bar{1}$11] direction) taken from the pure SnO_2 reference material. It can be seen that the particle size of pure SnO_2 is in the range of several to 30 nm and that SnO_2 has a cassiterite structure. The majority of the particles are single crystals and faceted with (110), ($\bar{1}$11), and (001) planes exposed. No twinned particles were found in this pure SnO_2 sample. Figures 2c and 2d are HREM images of the Sb_2O_3 and Sb_2O_5 reference materials taken along their [100] and [110] directions, respectively (with their basic lattice directions indicated by arrows in the images). The Sb_2O_3 and Sb_2O_5 powder materials were obtained from Aldrich and are composed of micron or submicron particles. Crystals in Sb_2O_3 have needle-like structures, while those in Sb_2O_5 have cubic structures. Selected-area electron diffraction analysis indicates that the Sb_2O_3 has an orthorhombic structure with its lattice parameters of $a = 0.493$ nm, $b = 1.248$ nm, and $c = 0.543$ nm (34). The Sb_2O_5 has a face-centered cubic structure with $a = 1.022$ nm (35).

Figure 3 shows HREM images taken from the ATO nanophase catalysts calcined at (a) 250°C, (b) 600°C, and (c) 1000°C, respectively. Notably, at 250°C, the catalyst is not well crystallized with small crystals ($\sim$5 nm) surrounded by amorphous material. The ATO catalyst calcined at 600°C contains well-crystallized larger particles ($\sim$10 nm). However, there is still a small amount of amorphous material at the edges of some nanoparticles. For the ATO catalyst calcined at 1000°C, the particle size becomes larger ($\sim$10–50 nm), and the catalyst is well crystallized without amorphous surface layers. It is notable that some twinned particles were observed in the catalyst calcined at this temperature, as indicated by the arrow in Fig. 3c. Figure 3d shows an HREM image of the twin viewed along a direction parallel to its twin plane. Analysis of the Fourier transform of the image (inset in Fig. 3d) shows this particle is a (101) twin, consistent with previous observations of ATO catalysts by other groups (18–19). HREM observations also indicate that most particles facet with their (110), (100), and (001) planes exposed. This observation agrees

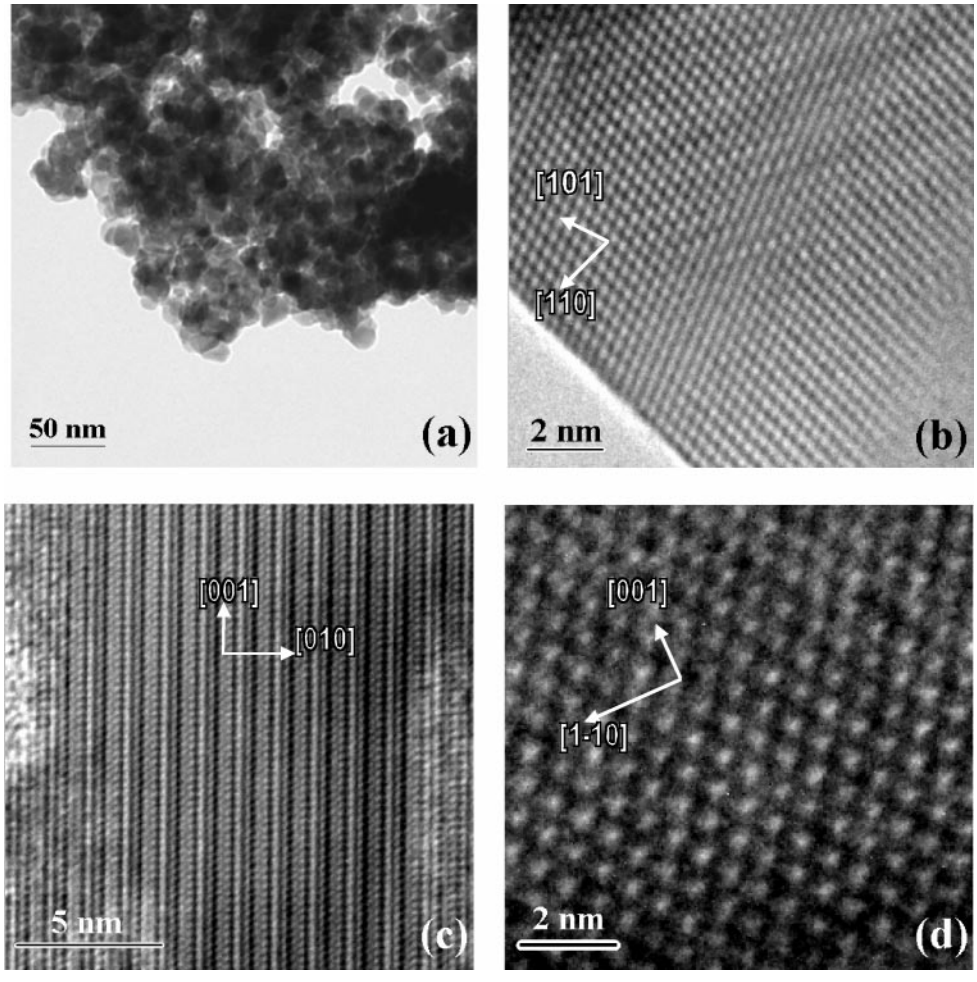

FIG. 2. (a) Low magnification and (b) HREM images (viewing along its [$\bar{1}$11] direction) of pure SnO_2. (c) and (d) HREM images of Sb_2O_3 viewing along its [100] axis and Sb_2O_5 along its [110] direction, respectively.

with simulations, which suggested that these three planes were the most thermodynamically stable (21).

3.2. Z-Contrast Imaging and EELS Results

Figures 4a and 4b are low-loss and core-loss EEL spectra acquired for the SnO_2, and Figs. 4c and 4d are low-loss and core-loss spectra of the Sb_2O_3 and Sb_2O_5 reference materials. The core-loss spectra were obtained by processing the experimental spectra in the following manner: several experimental spectra were acquired using short acquisition times and summed up to increase the signal-to-noise ratio. The background of the summed up spectra was then removed by fitting the pre-edge to a power law function of the form AE^r (where E is the energy loss and A and r are constants) (23). To remove multiple scattering, this spectrum was deconvoluted by its corresponding low-loss spectrum using the Fourier ratio method. Finally, all spectra were normalized to the continuum interval 30 eV after $M_{4,5}$ edges (630–660 eV).

The main feature of the low-loss spectrum of the SnO_2 is that it contains the $Sn:N_{4,5}$ peak and peaks at energies of 12 and 20 eV, respectively. The spectra for Sb_2O_3 and Sb_2O_5 are similar except that plasmon (at 21 eV) shapes are different; however, *they are* both readily identifiable from the SnO_2 spectrum. The main features of the core-loss spectra of these three reference materials are that they are composed of two sharp oxygen K peaks (marked as ***A*** and ***B***) overlapping with delayed $Sn:M_{4,5}$ for SnO_2 or $Sb:M_{4,5}$ (marked as ***C***) for both Sb_2O_3 and Sb_2O_5. Using the carbon K edge (284 eV) to calibrate the EEL spectra, we identified the ***A*** peak positions in the oxygen K edge at 540 eV for all three reference materials. The ***B*** peak position is 546.5 eV for SnO_2, 545.5 eV for Sb_2O_3, and 543.5 eV for Sb_2O_5. The ***C*** peak is 562 eV for SnO_2, while those for the Sb_2O_3 and Sb_2O_5 are 572 and 576 eV, respectively. The oxygen ***A*** peaks of SnO_2 and Sb_2O_5 have lower intensities than ***B*** peaks, while the ***A*** peak of Sb_2O_3 has a higher intensity than the ***B*** peak. Normally, for a semiquantitative interpretation of a spectrum to obtain the valence states, it

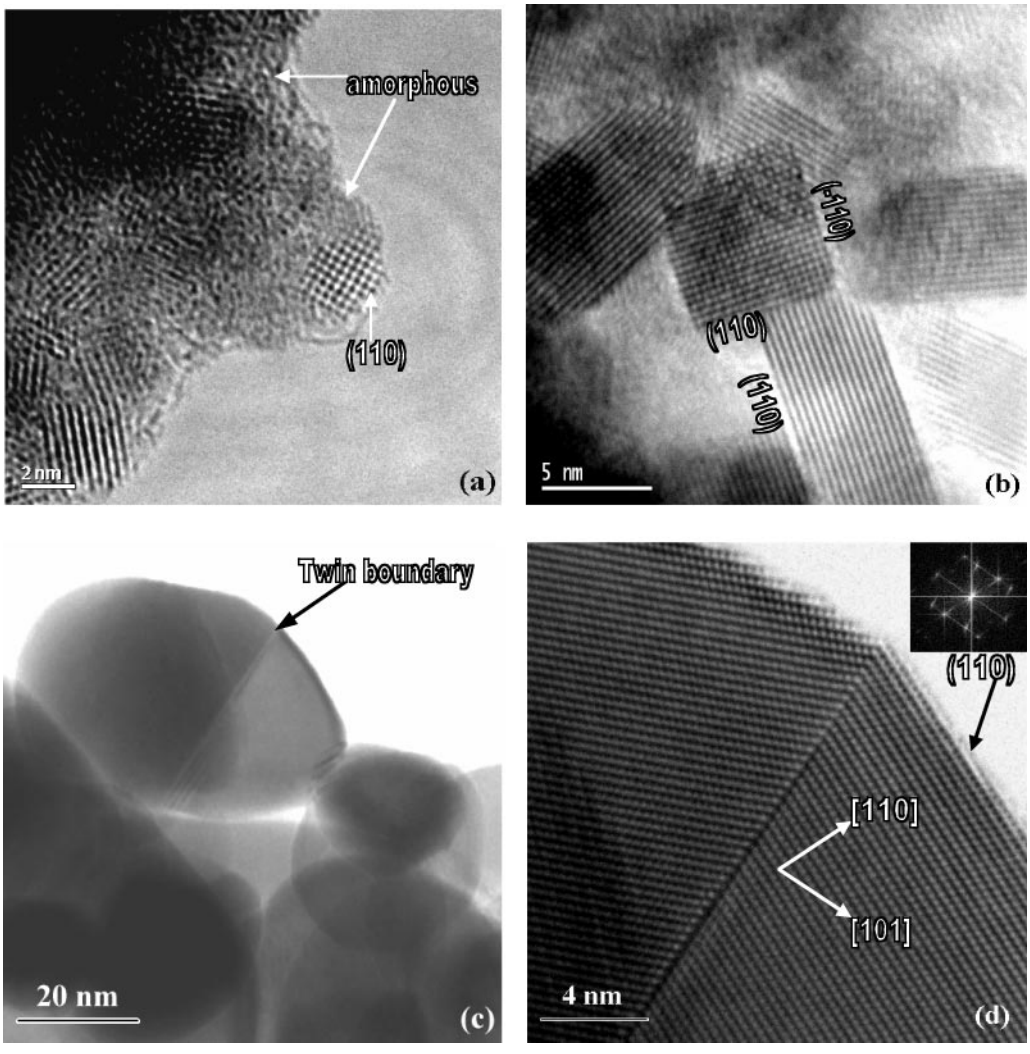

FIG. 3. (a) and (b) HREM images of the ATO catalysts calcined at 250 and 600°C, respectively. (c) Low magnification image of the ATO calcined at 1000°C showing a twinned particle. (d) HREM image of the twinned particle. Its Fourier transform is inserted in the upper right corner.

is important to know the energies and the relative intensities of each of the peaks in the spectrum. The spectrum acquired from SnO_2 consists of an oxygen K edge (532 eV) and tin $M_{4,5}$ edges (482 eV). They overlap together. In the spectra acquired from antimony oxides, the oxygen K edge overlaps with antimony $M_{4,5}$ edges (524 eV). This makes their interpretation complicated. Nevertheless, the differene between the spectrum acquired from Sb_2O_5 and that from Sb_2O_3 indicates that these spectra can still be used as "fingerprints" to identify the presence of Sb (III) and Sb (V) and their distribution in the ATO catalysts.

Z-contrast images taken from the ATO catalysts calcined at 250, 600, and 1000°C are shown in Figs. 5a, 5b, and 5c, respectively. The brightest spots in the *Z*-contrast image shown in Fig. 5b correspond to atomic columns. As Sn ($Z = 50$) and Sb ($Z = 51$) are neighbors in the Periodic Table, they cannot be separated from each other in the *Z*-contrast images. This means that *Z*-contrast images alone cannot give accurate information regarding Sb distribution. However, they can be used not only for EELS collection but also for beam damage monitoring. By placing the electron probe at the centers and edges of the particles in the images, center and edge EEL spectra can be obtained. Figures 5d–f show the processed EEL spectra acquired from these ATO catalysts calcined at 250, 600, and 1000°C, respectively. These spectra were obtained using the same procedures as those used for the reference spectra. All the spectra were calibrated using carbon K edge, which gives the peak positions of peaks ***A***, ***B***, and ***C*** of the edge and center spectra among the ATO catalysts as shown in Table 1. It can be seen that at the 250°C calcining temperature there is not much difference between the center and

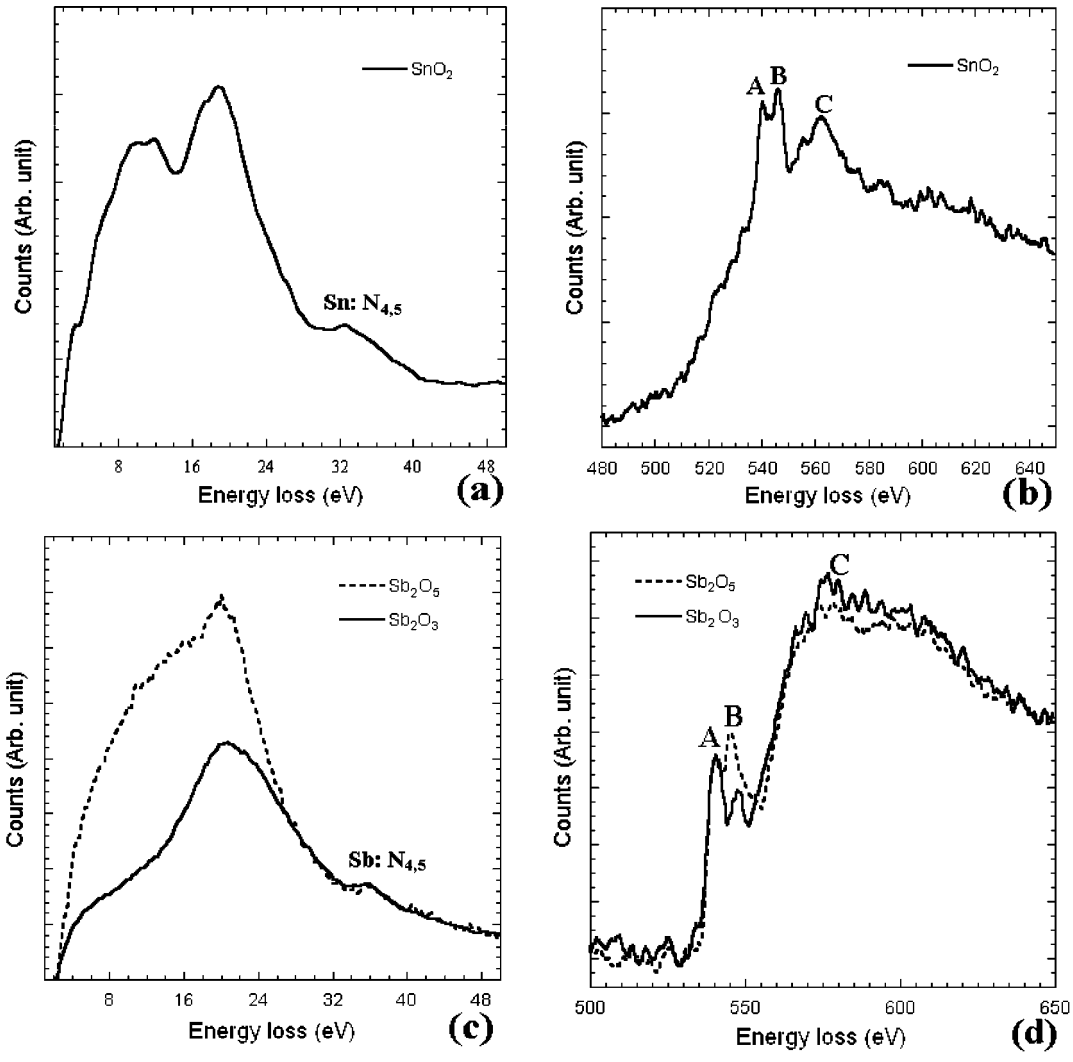

FIG. 4. Processed (a) low-loss and (b) core-loss spectra acquired from the pure SnO_2. (c) Low-loss and (d) core-loss spectra of the Sb_2O_3 and Sb_2O_5, respectively.

the edge spectra. They both show that the ***A*** peaks have less intensity than the ***B*** peaks and that the ***C*** peaks have similar positions. For the ATO calcined at 600°C, the ***A*** peak of the edge spectrum has a higher intensity than that of the ***B*** peak, while the ***B*** peak of the center spectrum has a higher intensity than that of the ***A*** peak. Also it seems that the ***C*** peak of the edge spectrum has a lower energy than that of the center spectrum. The main features of both the center and the edge spectra of the ATO calcined at 1000°C are that the ***A*** peaks have lower intensities than those of the ***B*** peaks, while the intensity difference between the ***A*** and ***B*** peaks in the edge spectrum is smaller than that in

TABLE 1

Peak Positions of the ATO Catalysts and Reference Materials[a]

	ATO calcined at 1000°C		ATO calcined at 600°C		ATO calcined at 250°C		Reference materials		
Peaks (eV)	Edge	Center	Edge	Center	Edge	Center	SnO_2	Sb_2O_3	Sb_2O_5
A	537.5	538.5	539.5	540	540.5	540.5	540	540	540
B	544	545	545	545.5	546	546	546.5	545.5	543.5
C	562	564	566	571	570	570	562	572	576

[a] Calibrated by carbon K edge, $\Delta E = \pm 1.5$ eV.

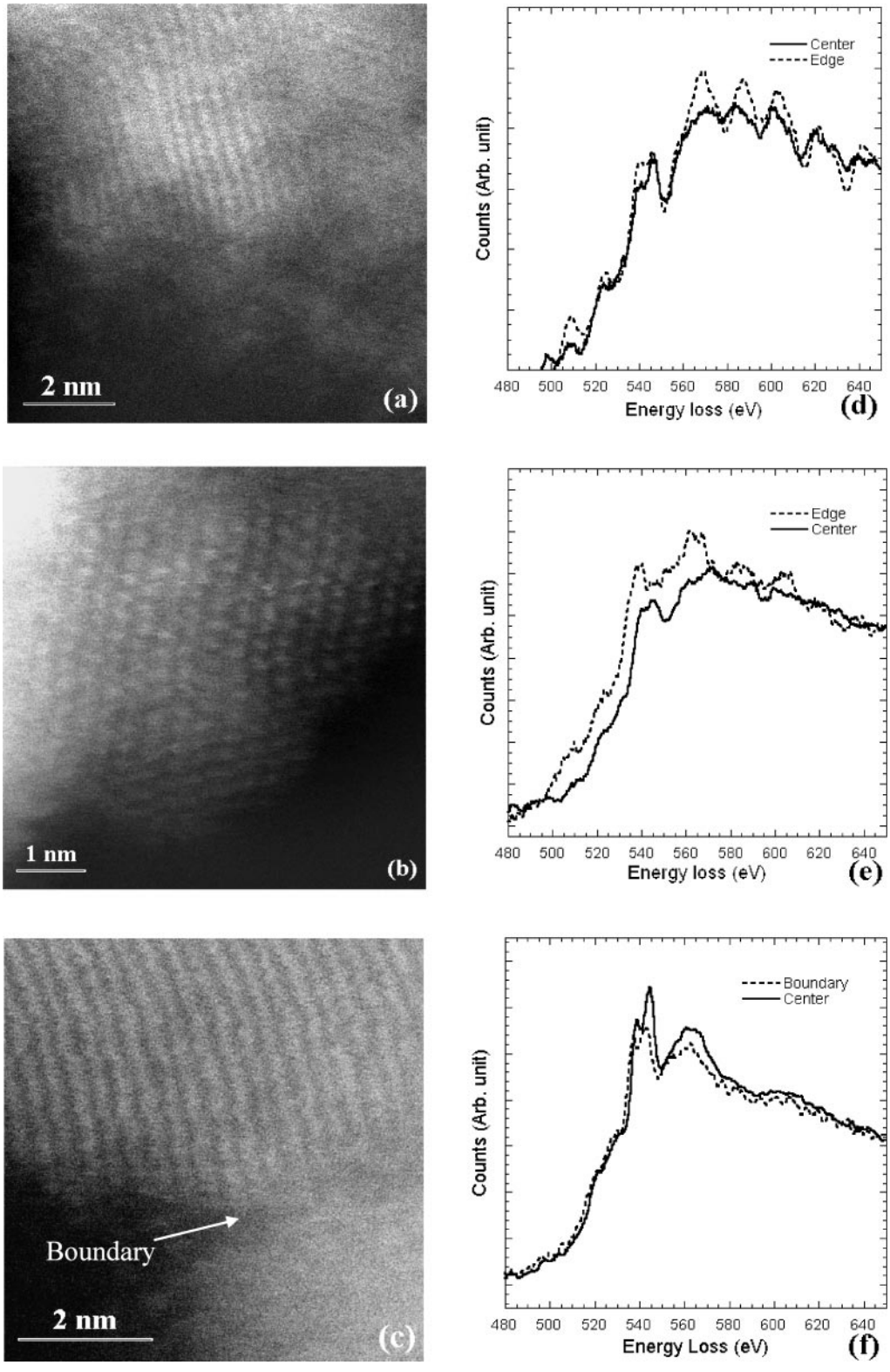

FIG. 5. *Z*-contrast images taken from the ATO catalysts calcined at (a) 250°C, (b) 600°C, and (c) 1000°C, respectively. (d), (e), and (f) Processed EEL spectra taken from the particles in (a), (b), and (c), respectively.

the center spectrum. The ***C*** peak of the edge spectrum has a lower energy than that of the center spectrum. As mentioned earlier, due to the overlaps of the edges, it will be difficult to interpret these spectra based on these "fine" structures.

4. DISCUSSION

The concepts, "edge" and "center" spectra instead of "surface" and "bulk" spectra, are used here in describing the EELS results, as when EELS is performed in the transmission mode, real "surface" spectra can only be acquired from exact edge-on particles. Pure "bulk" spectra are impossible to acquire as electrons passing through the center of a particle, crossing two surface layers and the bulk material. This means the "center" spectra should contain contributions from both surfaces and from the bulk structure. To obtain information on the bulk we therefore needed to determine the ratios of bulk atoms to surface atoms for particles with different sizes. Considering that most particles in the ATO catalysts are facetted with some special planes exposed, we constructed several simple crystal models. As shown in Table 2, four different particles with sizes of $2 \times 2 \times 2$ nm, $5 \times 5 \times 5$ nm, 10×10 nm, and $50 \times 50 \times 50$ nm, respectively, were considered to represent typical particle sizes of the three ATO catalysts we studied. Assuming that the EEL spectra were collected with electrons passing through the particles along either the [001] ($d = 0.319$ (0.159) nm) or the [$\bar{1}$11] ($d = 0.231$ nm) direction (which corresponds to our imaging conditions), and surface atoms occupy only several atomic layers, e.g., three atomic layers here, the surface/bulk ratios were calculated (shown in Table 2). It can be seen that when the particle sizes were larger than 5 nm, the center spectra were dominated by contributions from bulk atoms. In fact, if the particles were smaller than 2 nm, nearly all atoms lay on the surface. The experimental spectra in this study were collected from particles about 5 nm in diameter or larger, so that the center spectra could, to a first approximation, be treated as bulk spectra. This means that by analyzing these center and edge spectra, Sb valence states and distribution as a function of temperature could be determined.

To evaluate the distribution of antimony ions in the ATO catalysts, a MLLS method was used for fitting the experimental spectra using the reference spectra (plotted in Fig. 6) (23). This method is suitable for interpreting noisy spectra and spectra containing overlapped edges. Figures 6a and 6b show the experimental edge and center spectra of the ATO catalyst calcined at 1000°C together with MLLS fitted spectra. In Fig. 6a the MLLS fitted spectrum was obtained by fitting the experimental edge spectrum using the standard spectra of Sb_2O_3 and SnO_2. In this case, the reference spectrum of Sb_2O_5 resulted in a negative weighting factor, therefore it was not used in the fitting procedure. In Fig. 6b, the experimental spectrum could only be fitted by the spectra of SnO_2 and Sb_2O_5, while if Sb_2O_3 were considered we would have obtained a negative weighting factor. We also found that both the edge and the center spectra from some particles could not be fitted by the spectra of Sb_2O_3 and/or Sb_2O_5 together with the spectrum of SnO_2. This may imply either that there is much less antimony in some particles or that the distribution of antimony in the ATO catalysts is inhomogeneous.

Figures 6c and 6d are the experimental edge and center spectra of the ATO catalyst calcined at 600°C together with the MLLS fitted spectra. Similarly, the edge spectrum could only be fitted by the reference spectra of Sb_2O_3 and SnO_2, while the center spectrum could only be fitted by the spectra of SnO_2 and Sb_2O_5.

Figures 6e and 6f are the experimental edge and center spectra of the ATO catalyst calcined at 250°C together with the MLLS fitted spectra. In this case, the edge spectrum could be fitted mainly by the reference spectra of Sb_2O_5 and SnO_2, and if Sb_2O_3 were considered, it would have had a very small weighting factor. The center spectrum could only be fitted by the spectra of SnO_2 and Sb_2O_5.

These results semiquantitatively confirm that Sb (III) is generated and segregates to the surface of ATO nanoparticles as the calcination temperature is increased. The lower oxygen **A** and **B** peaks' intensities of the experimental spectra of the ATO calcined at 250 and 600°C than those of the MLLS fitted spectra may be due to the fact that the surfaces of these two samples contain a high degree of amorphous material (24, 36). The Sn/Sb ratios in the edge and center of the ATO catalysts calcined at different temperatures were obtained by MLLS fitting (shown in Table 3). It can be seen that the solubility of Sb in well-crystallized SnO_2 is no more than 5%. This is consistent with previous results (no more than 4%) (15).

Separated antimony oxides were also found by EELS in the ATO catalyst calcined at 600°C, while XRD only detected separate antimony oxide phases in the ATO materials calcined at 1000°C. That there are fewer separated antimony oxides formed at 600°C implies that EELS is more sensitive than X-ray techniques in detecting a small amount of second inclusions. Figure 7a shows the low-loss spectrum and Fig. 7b shows the experimental and MLLS fitted core-loss spectra of the antimony oxide phase. The low-loss spectrum which has a plasmon energy of 16 eV is not similar to the low-loss spectra of either Sb_2O_3 or Sb_2O_5. The fitted

TABLE 2

Surface/Bulk Ratios of Particles with Different Sizes Viewing Along Different Directions

Viewing directions	Surface/bulk ratios of particles with different sizes (nm)			
	$2 \times 2 \times 2$	$5 \times 5 \times 5$	$10 \times 10 \times 10$	$50 \times 50 \times 50$
[001]	≈1/1	≈1/4	≈1/9	≈1/51
[$\bar{1}$ 11]	≈2/1	≈1/3	≈1/6	≈1/35

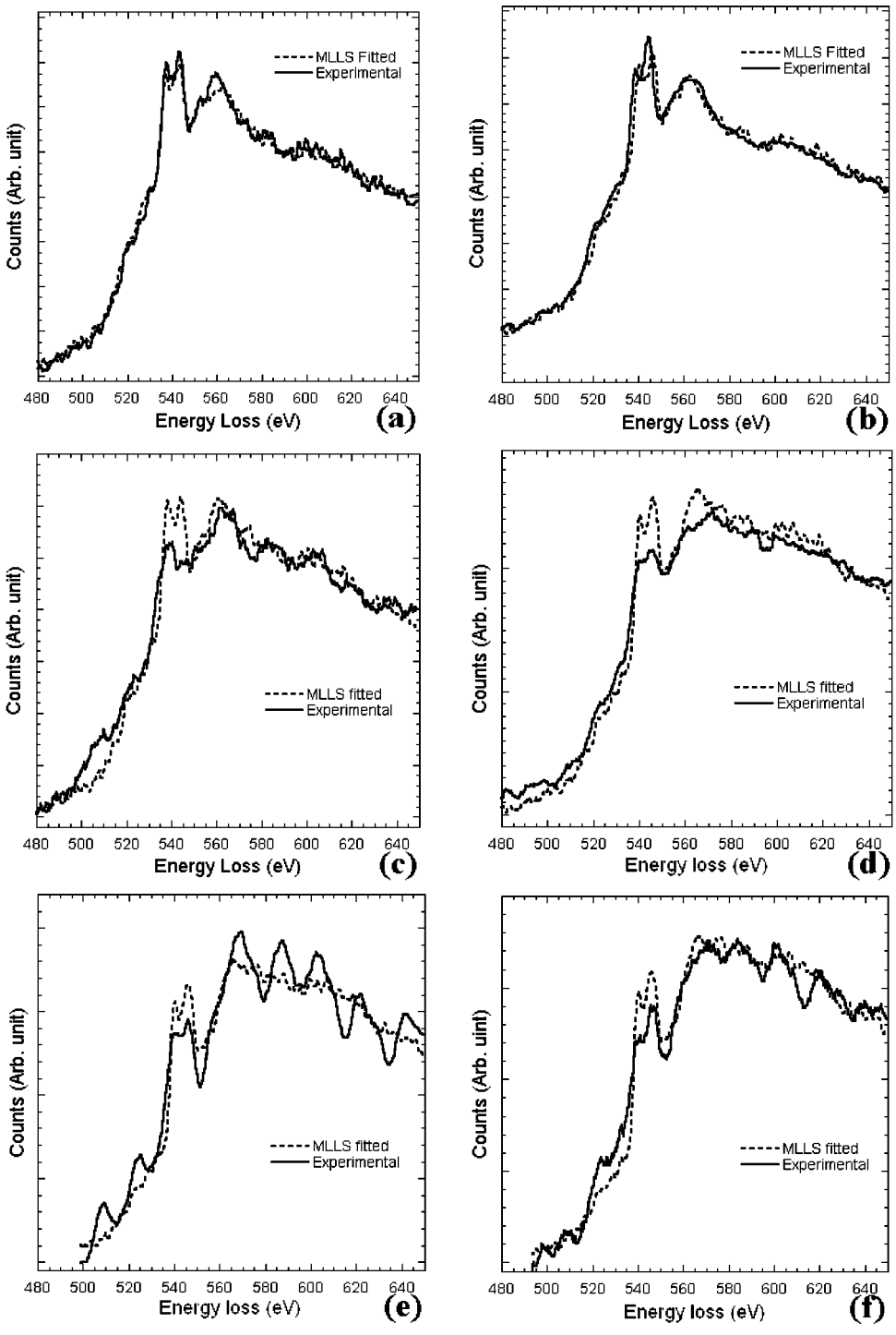

FIG. 6. (a) and (b) Experimental and MLLS fitted edge and center spectra of the ATO calcined at 1000°C. (c) and (d) Experimental and MLLS fitted edge and center spectra of the ATO calcined at 600°C. (e) and (f) Experimental and MLLS fitted edge and center spectra of the ATO calcined at 250°C, respectively.

spectrum was obtained by MLLS fitting using the standard spectra of Sb_2O_3 and Sb_2O_5 which give an Sb (III)/Sb (V) ratio of 2.4/1. This suggests that this phase contains both Sb (III) and Sb (V) species in its structure. It may be the Sb_2O_4 phase in which Sb exists as two different oxidation states, Sb (III) and Sb (V) (37). The Sb (III)/Sb (V) ratio in the reported Sb_2O_4 phase is 1.6/1 (37). This means that more Sb (III) ions are contained in the observed Sb_2O_4 phase in the

TABLE 3

Sn/Sb Ratios in ATO Catalysts Calcined at Different Temperatures Obtained by MLLS Fitting

	ATO calcined at 1000°C		ATO calcined at 600°C		ATO calcined at 250°C	
Samples	Edge	Center	Edge	Center	Edge	Center
Sn/Sb ratios	Sn/Sb (III) 18/1	Sn/Sb (V) 31/1	Sn/Sb (III) 3.4/1	Sn/Sb (V) 6/1	Sn/Sb (V) 1/1.2	Sn/Sb (V) 1.1/1

ATO calcined at 600°C, which may be caused by the charge balance for oxygen vacancies (inferred from the lower intensity in the oxygen K edges). This may explain why the oxygen peaks in the experimental spectrum have a lower intensity than those in the MLLS fitted spectrum (24, 36).

There are several different viewpoints on the active sites of the ATO catalysts described in the literature: (i) isolated Sb (III) species surrounded entirely by Sn (IV) nearest neighbors (12), (ii) the surface Sb (III)–Sb (V) couples (38), (iii) the surface Sn (II) + vacancy complex and Sb (III) + vacancy complex (8), (iv) an oriented film of Sb_2O_4 supported by the Sb (V)/SnO_2 solid solution (5), and (v) surface Sb (V) species (39). Our results show that antimony exists mainly as a Sb (III) state in the surface of these catalysts calcined at higher temperatures. At higher temperatures, Sb (V) transforms into Sb (III) probably by the Sb (V) + V_o = Sb (III) (V_o, oxygen vacancy) mechanism. This means that Sb (III) sites in the surface are coordination unsaturated sites (40). Coordination unsaturated sites play an important role in oxide catalyst performance, because reactants may bind to these sites and become activated for catalytic conversion. This has been directly verified recently by low-energy electron diffraction (LEED) and scanning tunneling microscopy (STM) on an atomic scale (41). So, the surface-segregated Sb (III) ions may act as active sites in ATO catalysts (12). We did not find surface Sb_2O_4 layers in ATO calcined at higher temperatures, although Sb_2O_4 separated particles were found even in the sample calcined at 600°C. However, previous reports have ruled out the possibility of the Sb_2O_4 phase in ATO catalysts acting as active sites because of its low activity (even though it has good selectivity) (10). Recent research on $SbVO_4/Sb_2O_4$ catalysts showed no improvement in the activity to acrylonitrile from the mechanical mixing of Sb_2O_4 and $SbVO_4$ catalysts, while the presence of the Sb_2O_4 phase formed during the synthesis of the catalyst enhanced selectivity to more than a factor of 2 (42). Considering the similarity between the Sn(Sb)O_2 and the $SbVO_4$ systems, which are all-important industrial catalysts used for selective oxidations, the Sb_2O_4 phase formed during calcination in the ATO catalysts may also contribute to the selectivity of the ATO catalysts.

Compared to other techniques such as XAS and HREELS, EELS performed in an electron microscope has been much less utilized for the characterization of catalysts. This may be partly due to "fears" of electron beam damage effects. However, for the samples studied here this does not

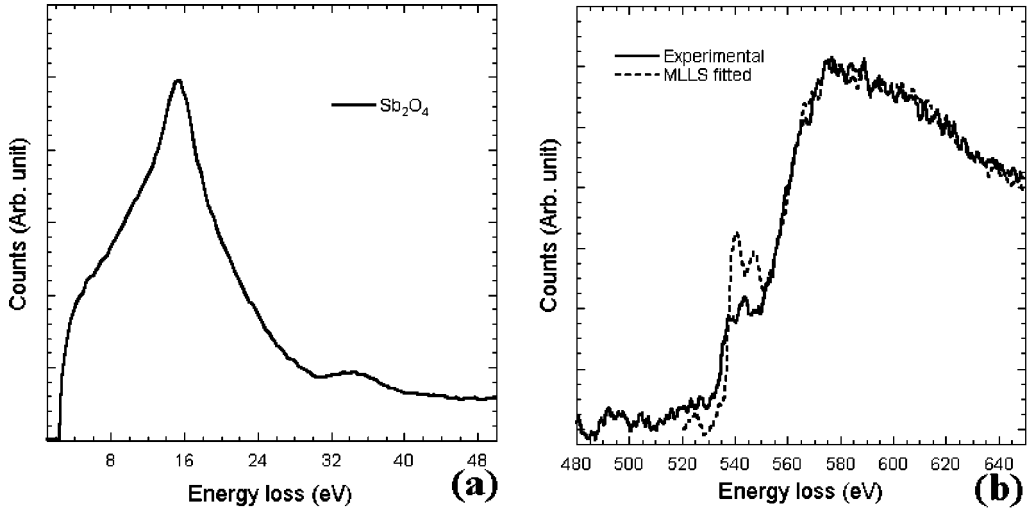

FIG. 7. (a) Low-loss spectrum of Sb_2O_4 phase formed at the calcination temperature of 600°C. (b) Processed experimental and MLLS fitted core-loss spectra of the antimony oxide.

seems to be a limiting case. For ionic materials, the knock-on or charge effect is a possible beam-damage mechanism (43). If Sb_2O_5, which is the most beam-sensitive material among those studied, were to undergo knock-on or charge, the Sb (V) would turn into Sb (III) by either Sb (V) + V_o = Sb (III) or Sb (V) + e = Sb (III) mechanisms, which would make the relative intensities of the oxygen **A** and **B** peaks change. However, by comparing spectra collected at the spot mode and by scanning a large area, we found beam damage to be negligible in the spectra used for our analysis (with a probe size of 0.2 nm and a beam current of 15 pA). Also it was reported that the features presented in their low-loss spectra, which suggest the presence of various Sn species, are Sn—10 and 14 eV; SnO—9, 13.5, and 27 eV; and SnO_2—12 and 20 eV (44). The features of low-loss spectra collected from the SnO_2 show main peaks at 12 and 20 eV, which clearly show that beam damage can be decreased and even avoided. Provided much caution is taken, EELS performed in a STEM with a field emission gun can be used for characterization of such industrial catalysts composed of nanoparticles.

5. CONCLUSIONS

In conclusion, EELS combined with Z-contrast and HREM imaging showed that the particle size and crystallinity of the ATO catalysts increase with calcination temperature. Using the reference materials, EEL spectra from the ATO catalysts calcined at different temperatures are qualitatively interpreted. The results show that at 250°C, Sb mainly exists as Sb (V) and may be incorporated inside the SnO_2 lattice or in an amorphous-like phase surrounding the SnO_2 crystals. For the ATO catalysts calcined at 600°C, the spectra from the edges of the particles correspond to trivalent Sb (III), while the spectra from the centers correspond to pentavalent Sb (V). The main features from the ATO catalysts calcined at 1000°C are consistent with Sb (V) being incorporated inside the SnO_2 nanoparticles, while Sb (III) is present within their edges. The surface Sb (III) sites are proposed to be coordination unsaturated sites and may act as active sites during catalytic reactions. This is the first time that these techniques were used to characterize this type of metal oxide catalyst containing nanophase materials using correlated atomic resolution electron microscopic and spectroscopic techniques. It also demonstrated that EELS combined with Z-contrast imaging performed in a STEM/TEM is a suitable technique for characterizing industrial catalysts composed of nanoparticles.

ACKNOWLEDGMENTS

This research was supported by the Monsanto Company. The JEOL 2010F used in this research was partially funded by NSF through Grant DMR-9601792 and is operated by the Research Resources Center at UIC. The help provided by A. W. Nicholls, Y. Ito, R. F. Klie, and H. L. Serrano is gratefully acknowledged.

REFERENCES

1. Caldadararu, M., Popa, V. T., Sprînceana, D., and Ionescu, N. I., *Appl. Catal. A* **125**, 247 (1995).
2. Seiyama, T., Egashira, M., Sakamoto, T., and Aso, I., *J. Catal.* **24**, 76 (1972).
3. Berry, F. J., *Adv. Catal.* **30**, 97 (1981).
4. Christie, J. R., Taylor, D., and McCain, C. C., *J. Chem. Soc., Faraday Trans. 1* **72**, 334 (1976).
5. Boudeville, Y., Figueras, F., Forissier, M., Portefaix, J. L., and Vedrine, J. C., *J. Catal.* **58**, 52 (1979).
6. Cross, Y. M., and Pyke, D. R., *J. Catal.* **58**, 61 (1979).
7. Cox, P. A., Egdell, R. G., Harding, C., Patterson, W. R., and Tavener, P. J., *Sur. Sci.* **123**, 179 (1982).
8. Dusastre, V, and Williams, D. E., *J. Phys. Chem. B* **102**, 6732 (1998).
9. Egdell, R. G., Rebane, J., Walker, T. J., and Law, D. S. L., *Phys. Rev. B* **59**, 1792 (1999).
10. Portefaix, J. L., Bussière, P., Forissier, M., Figueras, F., Friedt, J. M., Sanchez, J. P., and Theobald, F., *J. Chem. Soc., Faraday Trans. 1* **76**, 1652 (1980).
11. Berry, F. J., and Laundy, B. J., *J. Chem. Soc., Dalton Trans.* 1442 (1981).
12. Berry, F. J., *J. Catal.* **73**, 349 (1982).
13. Caldararu, M., Thomas, M. F., Bland, J., and Spranceana, D., *Appl. Catal. A* **209**, 383 (2001).
14. Ono, T., Yamanaka, T., Kubokawa, Y., and Komiyama, M., *J. Catal.* **109**, 423 (1988).
15. Pyke, D. R., Reid, R., and Tilley, R. J. D., *J. Chem. Soc., Faraday Trans. 1* **76**, 1174 (1980).
16. Rockenberger, J., Felde, U. Z., Tischer, M., Tröger, L., Haase, M., and Weller, H., *J. Chem. Phys.* **112**, 4296 (2000).
17. Berry, F. J., and Greaves, C., *J. Chem. Soc., Dalton Trans.* 2447 (1981).
18. Pyke, D. R., Reid, R., and Tilley, R. J. D., *J. Solid State Chem.* **25**, 231 (1978).
19. Smith, D. J., Bursill, L. A., and Berry, F. J., *J. Solid State Chem.* **44**, 326 (1982).
20. Berry, F. J., and Smith, D. J., *J. Catal.* **88**, 107 (1984).
21. Slater, B., Richard, C., Catlow, A., Gay, D. H., Williams, D. E., and Dusastre, V., *J. Phys. Chem. B* **103**, 10,644 (1999).
22. James, E. M., and Browning, N. D., *Ultramicroscopy* **78**, 125 (1999).
23. Egerton, R. F., "Electron Energy Loss Spectroscopy in the Electron Microscope," 2nd edition. Plenum, New York, 1996.
24. Klie, R. F., and Browning, N. D., *Appl. Phys. Lett.* **77**, 3737 (2000).
25. Pennycook, S. J., and Jesson, D. E., *Phys. Rev. Lett.* **64**, 938 (1990).
26. Jesson, D. E., and Pennycook, S. J., *Proc. Roy. Soc. London, Ser. A* **441**, 261 (1993).
27. Jesson, D. E., and Pennycook, S. J., *Proc. Roy. Soc. London, Ser. A* **449**, 273 (1995).
28. Nellist, P. D., and Pennycook, S. J., *Ultramicroscopy* **78**, 111 (1999).
29. Pennycook, S. J., Jesson, D. E., and Browning, N. D., *Nucl. Instrum. & Methods* **96**, 575 (1995).
30. Browning, N. D., and Pennycook, S. J., *J. Phys. D* **29**, 1779 (1996).
31. Browning, N. D., Chisholm, M. F., and Pennycook, S. J., *Nature* **366**, 143 (1993).
32. Batson, P. E., *Nature* **366**, 727 (1993).
33. Browning, N. D., and Pennycook, S. J., *Microbeam Anal.* **2**, 81 (1993).
34. Svensson, C, *Acta Crystallogr. B* **30**, 458 (1974).
35. Dehlinger, U., *Z. Kristallografiya* **66**, 108 (1927).
36. Browning, N. D., Moltaji, H. O., and Buban, J. P., *Phys. Rev. B* **58**, 8289 (1998).

37. Orchard, A. F., and Thornton, G., *J. Chem. Soc., Dalton Trans.* 1238 (1977).
38. Volta, J. C., Benaichouba, B., Mutin, I., and Vedrine, J. C., *Appl. Catal.* **8**, 215 (1983).
39. Caldararu, M., Thomas, M. F., Bland, J., and Spranceana, D., *Appl. Catal. A* **209**, 383 (2001).
40. Burwell, R. L., Haller, G. L., Taylor, K. C., and Read, J. F., *Adv. Catal.* **20**, 1 (1969).
41. Over, H., Kim, Y. D., Seitsonen, A. P., Wendt, S., Lundgren, E., Schmid, M., Varga, P., Morgante, A., and Ertl, G., *Science* **287**, 1474 (2000).
42. Nilsson, J., Cánovas, A. L., Hansen, S., and Andersson, A., *Catal. Today* **33**, 97 (1997).
43. Haskel, D., Sarikaya, M., Qian, M., and Stern, E. A., *Micron* **30**, 185 (1999).
44. Hoflund, G. B., and Corallo, G. R., *Phys. Rev. B* **46**, 7110 (1992).